Engineering xxx (xxxx) xxx

Contents lists available at ScienceDirect

Engineering

journal homepage: www.elsevier.com/locate/eng

Research
Environmental Sustainability—Article

# Defective Nickle–Iron Layered Double Hydroxide for Enhanced Photocatalytic NO Oxidation with Significant Alleviation of $NO_2$ Production

Xiaoyu Li [a,1], Xiaoshu Lv [a,1], Jian Pan [c], Peng Chen [d], Huihui Peng [a], Yan Jiang [a], Haifeng Gong [a], Guangming Jiang [a,b,*], Li'an Hou [b,*]

[a] Engineering Research Center for Waste Oil Recovery Technology and Equipment, Ministry of Education, Chongqing Technology and Business University, Chongqing 400067, China
[b] State Key Laboratory of Water Environment Simulation, School of Environment, Beijing Normal University, Beijing, 100875, China
[c] Environmental Technology Innovation Center of Jiande, Hangzhou Bertzer Catalyst Co. Ltd, Hangzhou 310058, China
[d] Chongqing Key Laboratory of Green Synthesis and Application, College of Chemistry, Chongqing Normal University, Chongqing 401331, China

ARTICLE INFO

*Article history:*
Received 19 February 2023
Revised 20 June 2023
Accepted 25 June 2023
Available online xxxx

*Keywords:*
Vacancies
Layered double hydroxide
$NO^+$
Photocatalysis
NO removal

ABSTRACT

Photocatalysis offers a sustainable avenue for the oxidative removal of low concentrations of $NO_x$ from the atmosphere. Layered double hydroxides (LDHs) are promising candidate photocatalysts owing to their unique layered and tunable chemical structures, and the abundant hydroxide ($OH^-$) moieties on their surfaces that are hydroxyl radical ($^•OH$) precursors. However, inferior charge separation and limited active sites on an LDH hinder its practical applications. Herein, we developed a facile $N_2H_4$-driven etching (et) approach that introduces dual $Ni^{2+}$ and $OH^-$ vacancies ($Ni_v$ and $OH_v$) into NiFe-LDH nanosheets (referred to as NiFe-LDH-et) that facilitate improved charge-carrier separation and the formation of active Lewis acidic sites ($Fe^{3+}$ and $Ni^{2+}$ exposed at $OH_v$). In contrast to inert pristine LDH, NiFe-LDH-et actively removes NO when illuminated with visible light. Specifically, $Ni_{76}Fe_{24}$-LDH-et etched in 1.50 mmol·$L^{-1}$ $N_2H_4$ solution removes 32.8% of the NO from continuously flowing air (NO-feed concentration: ~500 parts per billion (ppb)) when illuminated with visible light, thereby outperforming most reported catalysts. Experimental and theoretical data reveal that the dual vacancies promote the production of reactive oxygen species ($^•O_2^-$ and $^•OH$) and the adsorption of NO on the LDH. *In-situ* spectroscopy revealed that NO is preferentially adsorbed at Lewis acidic sites, particularly exposed $Fe^{3+}$ sites, and then converted into $NO^+$ that is subsequently oxidized to $NO_3^-$ without the formation of any of the more toxic $NO_2$ intermediate, thereby alleviating risks associated with its production and emission.



## 1. Introduction

The consumption of considerable quantities of fossil fuels in China has resulted in large annual $NO_x$ emissions. Although many measures have been adopted to reduce the amount of $NO_x$ released into the atmosphere, the proportion of this gas in air still remains high. Developing technology capable of removing $NO_x$, even at parts per billion (ppb) levels, remains an important objective given that $NO_x$ is highly toxic, very mobile, and reactive [1,2]. In this respect, photocatalysis is regarded to be a promising technology for removing $NO_x$ given its green, effective, and sustainable features [3]. Many studies have shown that photocatalysis readily oxidizes $NO_x$ to nitrate, which is then transferred to the water phase for further treatment [4].

Catalysts form the core of photocatalysis technology [5–8]. The light is absorbed at the catalyst surface and converted into hot charge carriers that facilitate the direct oxidation of $NO_x$ or trigger the formation of more oxidative free radicals, such as $^•O_2^-$ and $^•OH$ that oxidize $NO_x$ [9,10]. Layered double hydroxides (LDHs) are a large family of two-dimensional (2D) inorganic layered host materials with the general $[M^{2+}_{1-x}M^{3+}_x(OH)_2]^{z+}(A^{n-})^{z/n}\cdot mH_2O$ formula (where M and A correspond to cations and interlayer anions, respectively). LDHs are effective photocatalysts owing to their layered structures, tunable chemical and band structures, and abundant surface $OH^-$ moieties [11–13]. Furthermore, many research groups have

* Corresponding authors at: Chongqing Technology and Business University, Chongqing 400067, China
*E-mail addresses:* jiangguangming@zju.edu.cn (G. Jiang), houla@cae.cn (L. Hou).
[1] These authors contribute equally to this work.

https://doi.org/10.1016/j.eng.2023.06.017


Please cite this article as: X. Li, X. Lv, J. Pan et al., Defective Nickle–Iron Layered Double Hydroxide for Enhanced Photocatalytic NO Oxidation with Significant Alleviation of $NO_2$ Production, Engineering, https://doi.org/10.1016/j.eng.2023.06.017

shown that the $OH^-$ on an LDH can be converted into oxidative $^{\bullet}OH$ radicals when trapped by photoexcited holes [14–16]. This feature enables LDH to deliver robust and steady photocatalytic performance, even in a water-deficient environment; consequently, LDHs are ideal photocatalysts for abating air pollution. Despite these advantages, developed LDH photocatalysts still show limited performance when illuminated by visible light, which is possibly due to low hot charge-carrier efficiency and few exposed active sites on their surfaces [12,14].

Vacancy engineering is an effective method for activating or promoting the performance of a photocatalyst, and including vacancies has been documented to improve its band structure. Furthermore, vacancies serve as trapping centers for one type of charge carrier, which promotes light absorbance and charge-carrier separation [17]. For example, Miao et al. [18] developed a polymeric carbon nitride (PCN) photocatalyst rich in $N_{3C}$ vacancies that enhance visible-light absorption and promote photoexcited charge-carrier separation. The defective PCN produced $H_2O_2$ 4.5 times more rapidly than pristine PCN. In addition, the vacancies in some systems are the actual active sites that efficiently adsorb and activate reactants. For instance, Wu et al. [19] recently reported significantly enhanced oxygen evolution reactions (OERs) on oxygen-vacancy-bearing and cation-vacancy-bearing NiFe-LDHs, respectively. Both groups demonstrated that the observed enhancements in activity originate from the superior adsorption of OER intermediates at vacancies. Many research groups have recently reported various strategies for constructing cationic, anionic, or dual vacancies on LDHs, and successfully developed photocatalytic systems for various reactions, including nitrogen-reduction [20], $CO_2$-reduction [21], formaldehyde-decomposition [22], and $NO_x$-oxidation [10,23–25] reactions. However, constructing vacancies, particularly cationic/anionic dual vacancies, on an LDH usually involves a complex or time/energy-intensive procedure that hinders the scaled use of LDHs in photocatalysis applications.

Herein, we report the development of a facile $N_2H_4$-based etching strategy for introducing $Ni^{2+}$ and $OH^-$ dual vacancies in NiFe-LDH under mild conditions. Notably, the etching process takes only 10 min, and the number of vacancies can be tuned by adjusting the $N_2H_4$ concentration. We investigated the optical properties and charge-separation and -transfer efficiencies of the defective NiFe-LDHs, and how defects affect photocatalytic performance for the oxidative removal of NO when illuminated by visible light. The reactive oxygen species (ROSs) generated during photocatalysis and the reaction pathway for NO oxidation were also examined. Finally, the roles played by the dual vacancies in the NiFe-LDH are discussed based on a combined spectroscopic and density functional theory (DFT) study.

## 2. Experimental section

### 2.1. Materials

All chemicals were of analytical grade. Nickel nitrate hexahydrate ($Ni(NO_3)_2{\cdot}6H_2O$) and formamide were purchased from the Chengdu Kelong Chemical Co., Ltd. (China). Ferric nitrate nonahydrate ($Fe(NO_3)_2{\cdot}9H_2O$), terephthalic acid (TA), and ethanol were purchased from the Shanghai Titan Scientific Co., Ltd. (China). Hydrazine hydrate ($N_2H_4{\cdot}H_2O$), silver nitrate ($AgNO_3$), and acetonitrile were provided by the Shanghai Aladdin Bio-Chem Technology Co., Ltd. (China).

### 2.2. Photocatalysts synthesis

NiFe-LDH was prepared following a previously reported co-precipitation method [17]. Typically, $Ni(NO_3)_2{\cdot}6H_2O$ (7.5 mmol) and $Fe(NO_3)_3{\cdot}9H_2O$ (2.5 mmol) were dissolved in mixture of deionized water (20 mL) and formamide solution (20 mL) with magnetic stirring for 10 min. The mixture was then heated to 80 °C and the pH of the solution was adjusted to ~10 using 2.5 $mol{\cdot}L^{-1}$ aqueous NaOH. NiFe-LDH was collected by centrifugation after 10 min, washed with deionized water, and then freeze-dried for 12 h. NiFe-LDH (~0.6 g) and a specific amount of $N_2H_4{\cdot}H_2O$ were dispersed in deionized water (30 mL) to construct vacancies on the LDH. The mixture was then heated to 70 °C, and maintained at that temperature for 10 min. The product was subsequently collected by centrifugation, washed with water/ethanol, and freeze-dried for 12 h. The $N_2H_4$ concentration was adjusted to 0.96, 1.50, and 2.64 $mmol{\cdot}L^{-1}$ to gain insight into how the $N_2H_4$ dose affects the number of vacancies.

### 2.3. Characterization

The crystal phase of the catalyst was examined by X-ray diffractometry (XRD) with Cu Kα radiation (D/max RA, Rigaku Co., Japan). The metal content in the catalyst was determined by inductively coupled plasma atomic emission spectrometry (ICP-AES; Agilent 5110, USA). Transmission electron microscopy (TEM) and high-resolution TEM (HRTEM) images were collected using a JEM-2010 microscope (JEOL, Japan), and photoluminescence (PL) spectra were obtained on an F-7000 spectrophotometer (HITACHI, Japan). Ultraviolet–visible (UV–vis) diffuse reflectance spectroscopy (DRS) was performed on a UV-2450 spectrometer (Shimadzu, Japan). Photocurrent testing and electrochemical impedance spectroscopy (EIS) were conducted using a CHI 660E electrochemical workstation (Chenhua, China) [26]. Electron paramagnetic resonance (EPR) spectra were acquired on an EMX PLUS spectrometer (Bruker, Germany). *In-situ* diffuse reflectance Fourier-transform infrared spectroscopy (DRIFTS) was performed on a Vertex 70v spectrometer (Bruker) [27]. NO temperature-programmed-desorption-mass (TPD-mass) testing was conducted using an AutoChem1 II 2920 instrument (Micromeritics, USA) [28].

### 2.4. Evaluating photocatalytic performance

The photocatalytic performance of various LDH samples for the removal of NO was evaluated under visible light in a sealed rectangular reactor (30 cm × 15 cm × 10 cm) (the apparatus is schematically shown in Fig. S1 in Appendix A). The catalyst (0.2 g) was dispersed in ethanol (10 mL) to form a catalyst suspension prior to testing that was then evenly pasted onto the surfaces of two 12 cm diameter culture dishes. The catalyst-loaded dishes were placed in the reactor, sealed, and then charged with flowing air containing ~ 500 ppb NO at a relative humidity of 45%–55%. The catalyst was illuminated with visible light using a 150 W commercial tungsten halogen lamp (note that the ultraviolet region was filtered out using an ultraviolet cut-off filter ($\lambda \geq 420$ nm)). The concentrations of NO and $NO_2$ in the outlet flow were tracked using a gas analyzer (42i-TL, Thermo Scientific, USA). The NO removal ratio ($\eta$) of each catalyst was calculated using: $\eta = (1 - C_t/C_0) \times 100\%$, where $C_t$ and $C_0$ are the concentrations of NO at reaction times $t$ and 0, respectively.

## 3. Results and discussion

### 3.1. Photocatalyst synthesis and characterization

Fig. 1(a) shows the $N_2H_4$-based etching strategy for producing defective NiFe-LDH (referred to as "NiFe-LDH-et"). In this strategy, $N_2H_4$ molecules attack the $[Ni^{2+}(OH)_6]$ moieties in NiFe-LDH to form soluble $Ni(N_2H_4)_x^{2+}$ species through displacement chemistry, which leaches away $Ni^{2+}$ and $OH^-$ to form dual vacancies in the

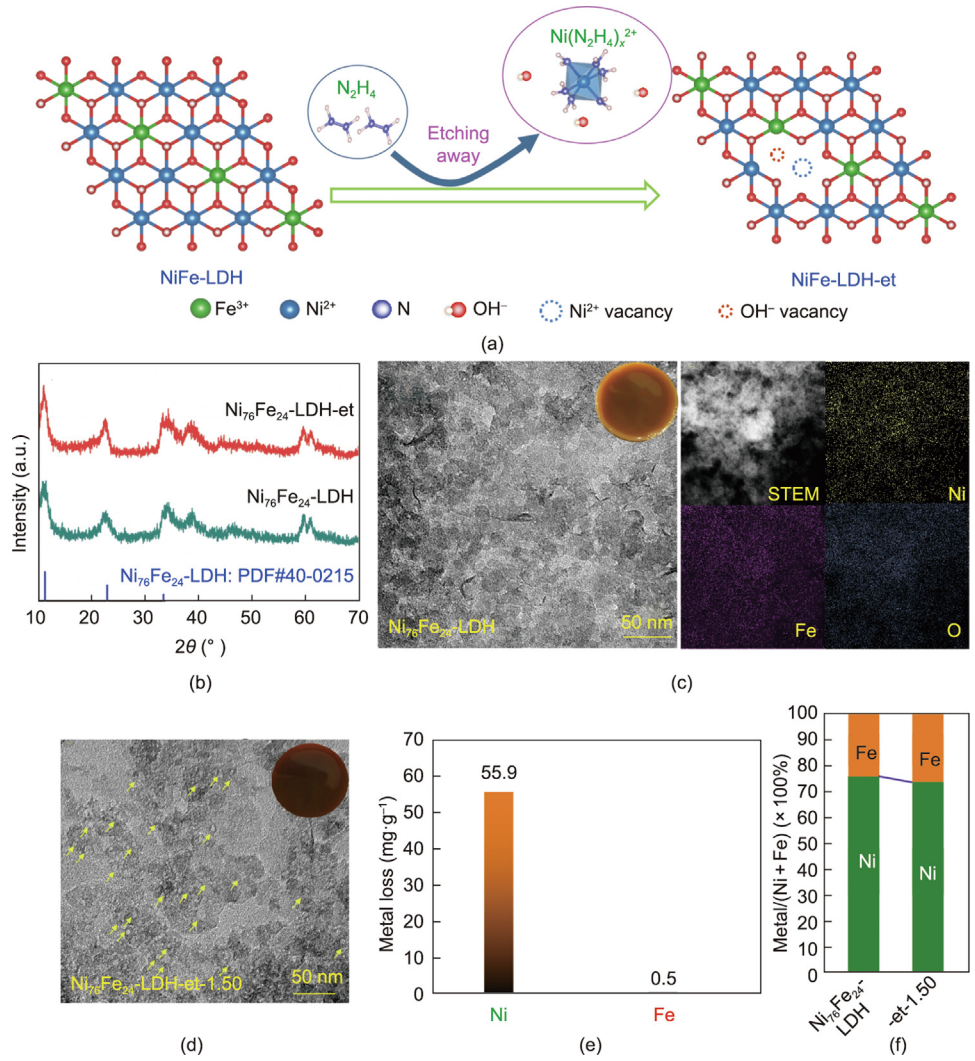


**Fig. 1.** (a) Schematical illustration of the procedure for synthesis of defective NiFe-LDH; (b) XRD patterns of the $Ni_{76}Fe_{24}$-LDH and $Ni_{76}Fe_{24}$-LDH-et; (c, d) TEM images of (c) $Ni_{76}Fe_{24}$-LDH and (d) $Ni_{76}Fe_{24}$-LDH-et (inset is the digital image of the samples that was pasted on the subface of a culture dish); (e) the concentrations of Ni and Fe leached in the $N_2H_4$ solution; (f) the molar ratio of Ni and Fe in the fine and etched $Ni_{76}Fe_{24}$-LDH.

LDH. The XRD patterns in Fig. 1(b) reveal that both pristine and defective $Ni_{76}Fe_{24}$-LDH possess the same hydrotalcite structure (PDF#40–0215), which implies that $N_2H_4$ etching does not destroy the LDH crystal structure. The photographic and TEM images in Fig. 1(c) and the atomic force microscope (AFM; BRUKER, Germany) image in Fig. S2 in Appendix A show that pristine $Ni_{76}Fe_{24}$-LDH is light brown in color and has a nanosheet morphology that is approximately 2.04–2.98 nm thick with a lateral dimension of 20–30 nm. Furthermore, Ni, Fe, and O are distributed evenly over the LDH sheet (Fig. 1(c)). In comparison, NiFe-LDH-et exhibits the same nanosheet morphology as pristine $Ni_{76}Fe_{24}$-LDH but is dark brown in appearance (Fig. 1(d)). Furthermore, a considerable number of nanopores were observed in the sheet (highlighted by yellow arrows) that indicate vacancy formation. The amounts of metals leached from $Ni_{76}Fe_{24}$-LDH and the metal content in $Ni_{76}Fe_{24}$-LDH-et were examined using ICP-AES. Fig. 1(e) reveals that 55.9 $mg \cdot g^{-1}$ of $Ni^{2+}$ and 0.50 $mg \cdot g^{-1}$ of $Fe^{3+}$ were leached when $Ni_{76}Fe_{24}$-LDH was treated with 1.50 $mmol \cdot L^{-1}$ aqueous $N_2H_4$. Furthermore, Fig. 1(f) shows that the Ni/(Ni + Fe) molar ratio decreases during etching, from the original value of 76% observed for LDH to 72% in LDH-et. Both sets of results demonstrate that $N_2H_4$ primarily etches away $[Ni^{2+}(OH)_x]$ moieties ($0 < x \leq 6$) rather than $[Fe^{3+}(OH)_x]$ moieties.

The defective structure of $Ni_{76}Fe_{24}$-LDH-et was further investigated using a combination of Raman (DRX, Thermo Scientific, USA) and EPR spectroscopies, along with X-ray photoelectron spectroscopy (XPS; K-Alpha, Thermo Scientific, USA). The Raman spectra in Fig. 2(a) show characteristic bands at 458, 526 and 705 $cm^{-1}$ that are ascribable to Fe/Ni–OH bond vibrations in $Ni_{76}Fe_{24}$-LDH; these bands weaken during etching with $N_2H_4$ [29–31]. Furthermore, a new band assigned to $OH^-$ vibrations in close proximity to cationic vacancies is observed at around 590 $cm^{-1}$ in the spectrum of $Ni_{76}Fe_{24}$-LDH-et [32,33]. Taken together, these results reveal that $N_2H_4$ etching induces the formation of cationic vacancies.

Conversely, EPR spectroscopy and XPS provide evidence for the formation of OH vacancies ($OH_v$). Both $Ni_{76}Fe_{24}$-LDH-et and $Ni_{76}Fe_{24}$-LDH display characteristic Lorentzian $OH_v$ signals at $g = 2.0048$ in their EPR spectra (Fig. 2(b)). The more intense signal observed for $Ni_{76}Fe_{24}$-LDH-et is suggestive of a higher number of $OH_v$ moieties following $N_2H_4$ etching, which is also supported by XPS. The O 1s spectra shown in Fig. 2(c) reveal that $Ni_{76}Fe_{24}$-LDH-et has an $OH_v$/lattice-$OH^-$ molar ratio (i.e., $O_v/O_l$) of 3.54, which is considerably higher than that determined for $Ni_{76}Fe_{24}$-LDH (2.12) [34–36].

The schematic in Fig. 2(d) shows that LDH structural evolution during $N_2H_4$ etching can form $OH_v$ sites that lie between $Ni^{2+}$ and

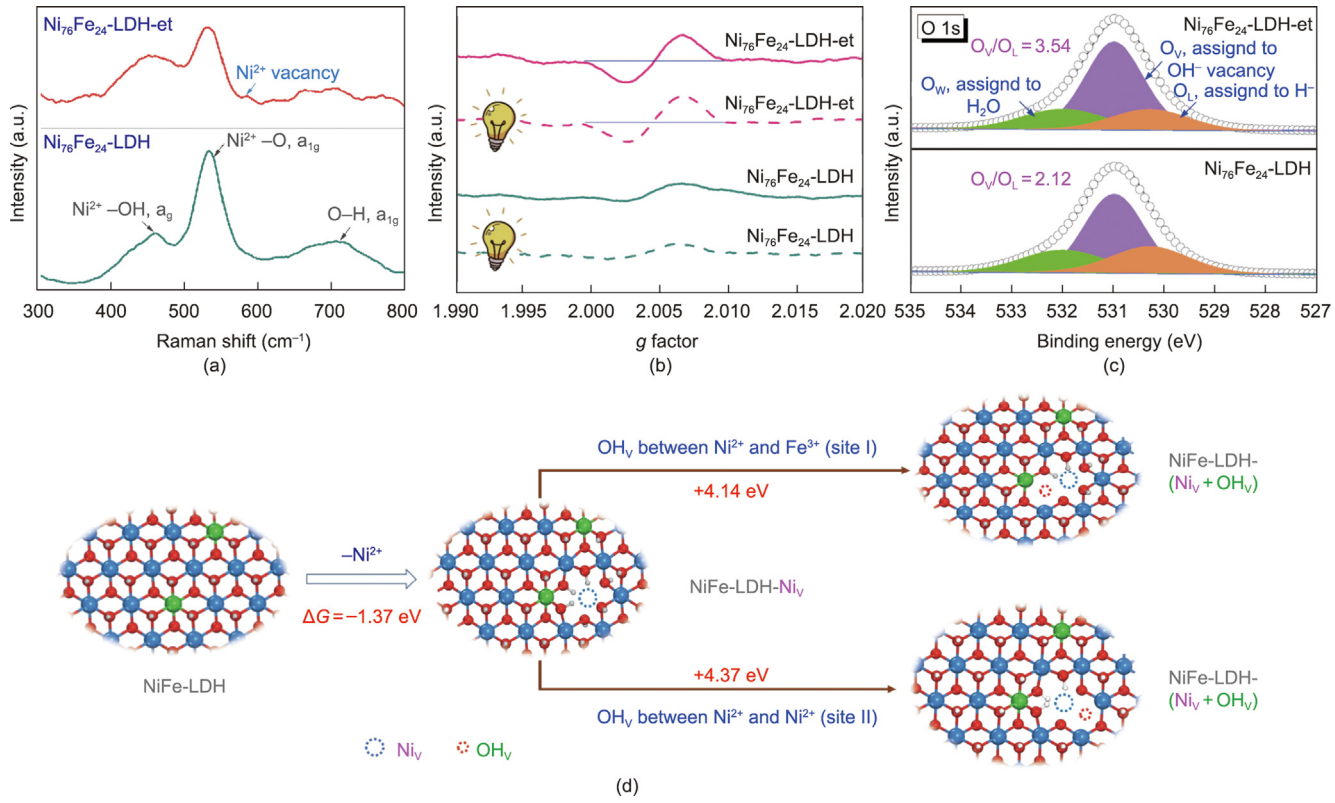


**Fig. 2.** (a) Raman spectra of $Ni_{76}Fe_{24}$-LDH and $Ni_{76}Fe_{24}$-LDH-et; (b) EPR spectra of $Ni_{76}Fe_{24}$-LDH and $Ni_{76}Fe_{24}$-LDH-et with and without the light irradiation; (c) O 1s XPS results of $Ni_{76}Fe_{24}$-LDH and $Ni_{76}Fe_{24}$-LDH-et; (d) the schematic diagram of vacancy formation in LDH.

$Ni^{2+}$ (site I) or $Ni^{2+}$ and $Fe^{3+}$ (site II). Accordingly, we analyzed the Ni 2p and Fe 2p XPS spectra of $Ni_{76}Fe_{24}$-LDH-et to determine the $OH_v$ position, the results of which are shown in Fig. S3 in Appendix A; the figure reveals that the $Ni^{2+}$ in $Ni_{76}Fe_{24}$-LDH-et maintains its +2 valence, whereas $Fe^{3+}$ becomes electron-rich relative to that in $Ni_{76}Fe_{24}$-LDH. This enrichment is ascribable to the loss of $OH^-$, which provides additional electrons to the coordination-unsaturated $Fe^{3+}$. These results imply that $OH_v$ is mainly formed at site II.

Gibbs free energy changes ($\Delta G$) associated with the formation of $Ni_v$ and $OH_v$ at sites I and II were calculated using DFT to rationalize the aforementioned results (details are provided in the Section S1. In Appendix A). Intriguingly, the removal of $Ni^{2+}$ from LDH is calculated to be spontaneous, with a $\Delta G$ of −1.37 eV (1 eV = $1.602 \times 10^{-19}$ J, Fig. 2(d)), while the subsequent removal of $OH^-$ at both sites requires additional energy. $OH_v$ is more favorably formed at site II than at site I from a thermodynamic perspective (4.14 vs 4.37 eV), which is consistent with the XPS data that show that $OH^-$ positioned between $Ni^{2+}$ and $Fe^{3+}$ is more easily removed.

Given that $N_2H_4$ effectively forms dual vacancies, $Ni_{76}Fe_{24}$-LDH was next treated with solutions containing different concentrations of $N_2H_4$ (i.e., 0.96, 1.50, or 2.64 mmol·$L^{-1}$) to afford $Ni_{76}Fe_{24}$-LDH-et-*x* (*x* = 0.96, 1.50, or 2.64). The photographic images in Fig. S4 in Appendix A show that NiFe-LDH-et darkens with increasing $N_2H_4$ concentration. The TEM images in Fig. S4 reveal that the LDH sheets contain fewer pores when 0.96 mmol·$L^{-1}$ $N_2H_4$ was used and are almost fragmented following treatment with 2.64 mmol·$L^{-1}$ $N_2H_4$. The XRD patterns in Fig. S5 in Appendix A confirm that the LDH phase is conserved in all three systems. ICP-AES data (Table S1 in Appendix A) show that increasing amounts of $Ni^{2+}$ (from 6.14 to 55.9 and 88.1 mg·$g^{-1}$) leach from the LDH as the $N_2H_4$ concentration is increased from 0.96 to 1.50 and 2.64 mmol·$L^{-1}$, while only low amounts of Fe are lost (0.04–0.67 mg·$g^{-1}$), as expected.

### 3.2. Photocatalytic performance for the oxidative removal of NO

The photocatalytic performance of $Ni_{76}Fe_{24}$-LDH-et-*x* and $Ni_{76}Fe_{24}$-LDH for the oxidative removal of NO was evaluated in terms of the ability of each catalyst to remove NO from continuously flowing air (2.4 L·$min^{-1}$, humidity of 45%–55%) containing ~500 ppb NO when irradiated with visible light (details of the apparatus used and the testing procedure are provided in Fig. 3(a) and Fig. S1). Fig. 3(b) shows the ratio of the outlet NO concentration to the feed concentration ($C/C_0$) as functions of reaction time for the various catalysts. Pristine $Ni_{76}Fe_{24}$-LDH is inert when irradiated with visible light, as $C \approx C_0$. Impressively, all $Ni_{76}Fe_{24}$-LDH-et-*x* samples exhibited catalytic activity under visible light, as $C \ll C_0$ for all three systems. NO-removal efficiency was calculated using $(1 - C/C_0) \times 100\%$ with the $C/C_0$ values presented in Fig. 3(b); the results are shown in Fig. 3(c). $Ni_{76}Fe_{24}$-LDH-et-1.50 clearly delivers the highest NO-removal efficiency of 32.8%, followed by $Ni_{76}Fe_{24}$-LDH-et-0.96 and $Ni_{76}Fe_{24}$-LDH-et-2.64. Notably, Fig. 3(d) reveals that none of the $Ni_{76}Fe_{24}$-LDH-et catalysts produced notable amounts of $NO_2$, which is the most toxic molecule in the $NO_x$ family and has an atmospheric threshold concentration of 40 ppb (Level I in Ambient Air Quality Standards, GB 3095–2012); these low $NO_2$ yields suggest that $Ni_{76}Fe_{24}$-LDH-et can be used in very reliable and green photocatalytic NO-cleanup procedures [37]. The above results show that, while defects unlock the visible-light photocatalytic activity of NiFe-LDH, an appropriate defect content is required to maximize photocatalytic performance.

Table S2 in Appendix A shows that the developed $Ni_{76}Fe_{24}$-LDH-et-1.50 catalysts outperform most LDH catalysts reported in the literature in terms of NO-removal efficiency under closed reaction conditions. As an important catalyst descriptor for practical applications, the durability of $Ni_{76}Fe_{24}$-LDH-et-1.50 for photocatalytic NO removal was evaluated through repeated testing under the

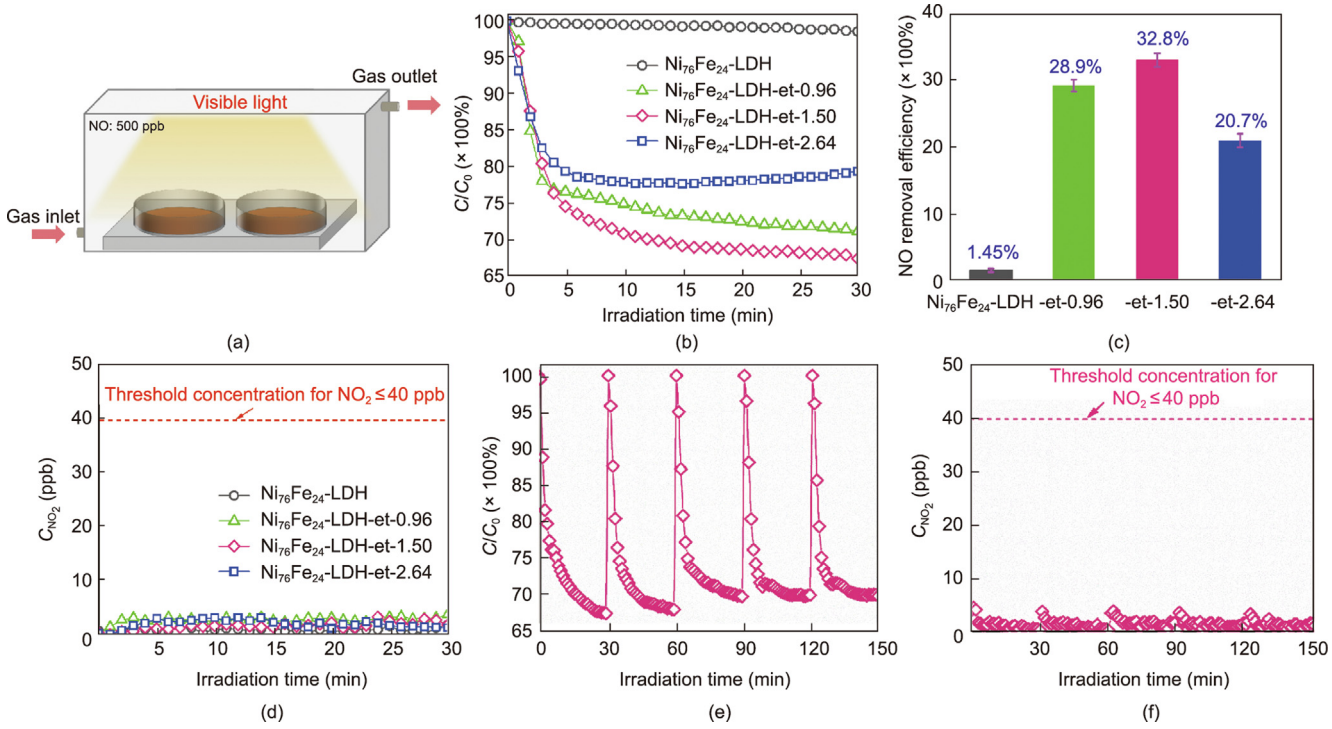


**Fig. 3.** (a) Schematic illustration of the reactor for photocatalytic NO oxidation; (b) The reaction time course of the $C/C_0$; (c) corresponding NO removal efficiency at the steady state; (d) the $NO_2$ yield during the photocatalytic NO oxidation on $Ni_{76}Fe_{24}$-LDH and $Ni_{76}Fe_{24}$-LDH-et-*x* (*x* = 0.96, 1.50, and 2.64); (e) $C/C_0$ profiles and the $NO_2$ yield during the durability test for the $Ni_{76}Fe_{24}$-LDH-et-1.50.

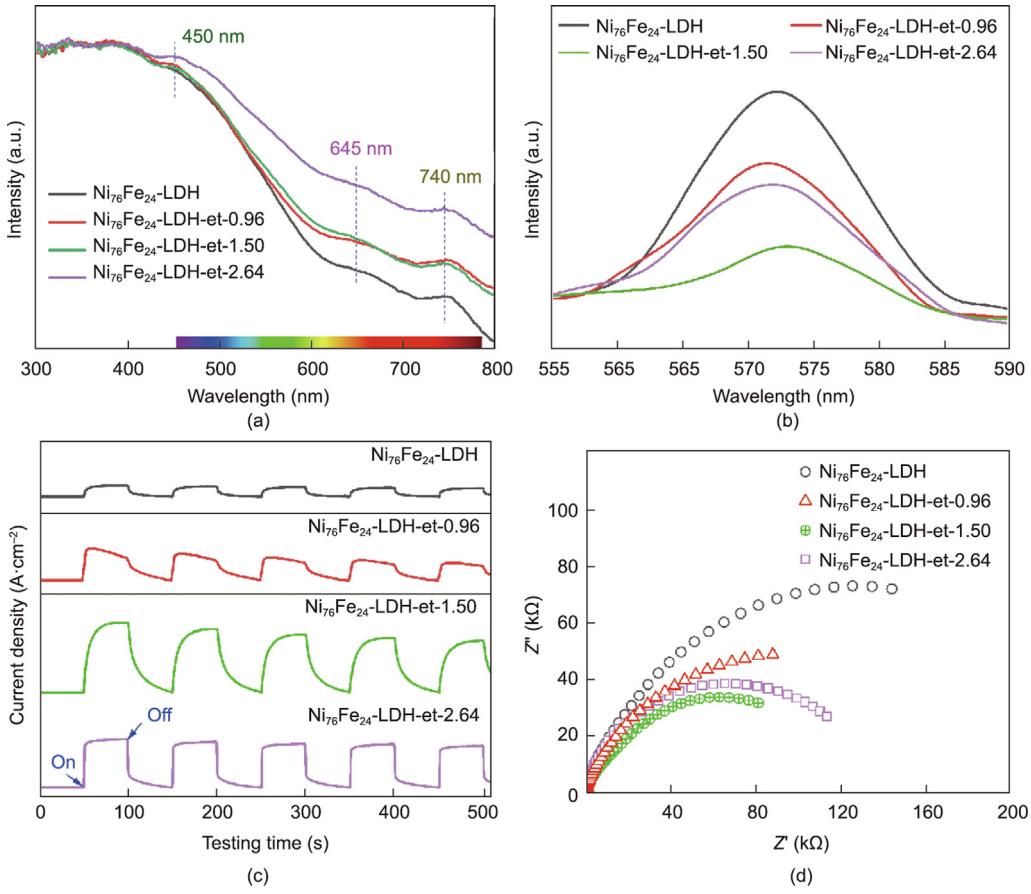


**Fig. 4.** (a) UV–Vis DRS spectra of $Ni_{76}Fe_{24}$-LDH and $Ni_{76}Fe_{24}$-LDH-et-*x* (*x* = 0.96, 1.50, and 2.64); (b) Room-temperature steadystate PL spectra of the $Ni_{76}Fe_{24}$-LDH and $Ni_{76}Fe_{24}$-LDH-et-*x* (*x* = 0.96, 1.50, and 2.64); (c) Transient photocurrent responses and (d) EIS of the $Ni_{76}Fe_{24}$-LDH and $Ni_{76}Fe_{24}$-LDH-et-*x* (*x* = 0.96, 1.50, and 2.64).

same reaction conditions. Figs. 3(e) and (f) show $C/C_0$ profiles that are similar in shape over five cycles of testing, with low $NO_2$ yields also observed. Furthermore, the XRD data presented in Fig. S6 in Appendix A show that the LDH crystal structure is preserved during repeated testing using $Ni_{76}Fe_{24}$-LDH-et-1.50. Taken together, these results imply that $Ni_{76}Fe_{24}$-LDH-et-1.50 exhibits long-term high photocatalytic performance.

### 3.3. Origin of the enhanced photocatalytic activity of NiFe-LDH-et

The activity of a photocatalyst is generally associated with its ability to absorb light, separate/transfer charges, and the number of reactive centers and their activities [38]. The light-absorbing efficiencies of $Ni_{76}Fe_{24}$-LDH and $Ni_{76}Fe_{24}$-LDH-et-*x* were first examined using UV–vis DRS. The spectra presented in Fig. 4(a) reveal that $Ni_{76}Fe_{24}$-LDH and $Ni_{76}Fe_{24}$-LDH-et-*x* absorb substantial amounts of visible light in the 400–800 nm wavelength range. However, the NiFe-LDH-et-*x* absorption edge was observed to gradually redshift with increasing *x*, which significantly enhanced adsorption in the 500–800 nm wavelength region. These results show that the introduction of vacancies in the LDH improves its ability to absorb visible light. As NiFe-LDH-et-2.64 performs most efficiently in the visible-light region but does not deliver peak NO-removal efficiency, we conclude that improved light adsorption is not principally responsible for the superior photocatalytic performance of NiFe-LDH-et.

The charge-separation efficiencies of $Ni_{76}Fe_{24}$-LDH and $Ni_{76}Fe_{24}$-LDH-et-*x* were investigated using PL spectroscopy. The PL spectra in Fig. 4(b) reveal that all $Ni_{76}Fe_{24}$-LDH-et-*x* samples exhibit lower PL intensities than $Ni_{76}Fe_{24}$-LDH owing to enhanced charge separation ascribable to the presence of vacancies in the LDH [3,39]. Furthermore, the PL intensity of the LDH exhibits a volcano-like relationship with *x*. $Ni_{76}Fe_{24}$-LDH-et-1.50 displayed the lowest PL intensity and, consequently, the highest photoexcited charge-carrier separation efficiency. The charge-transfer kinetics of $Ni_{76}Fe_{24}$-LDH and $Ni_{76}Fe_{24}$-LDH-et-*x* were evaluated by transient photocurrent response spectroscopy and EIS, respectively [40,41]. Fig. 4(c) shows that $Ni_{76}Fe_{24}$-LDH-et-1.50 delivers the highest photocurrent, followed by $Ni_{76}Fe_{24}$-LDH-et-2.64, $Ni_{76}Fe_{24}$-LDH-et-0.96, and $Ni_{76}Fe_{24}$-LDH; hence, the charge-transfer rate follows the order: $Ni_{76}Fe_{24}$-LDH-et-1.50 > $Ni_{76}Fe_{24}$-LDH-et-2.64 > $Ni_{76}Fe_{24}$-LDH-et-0.96 > $Ni_{76}Fe_{24}$-LDH; the same order was also determined by EIS. Fig. 4(d) shows that $Ni_{76}Fe_{24}$-LDH-et-1.50 exhibits the smallest EIS semicircle, followed by $Ni_{76}Fe_{24}$-LDH-et-2.64, $Ni_{76}Fe_{24}$-LDH-et-0.96, and $Ni_{76}Fe_{24}$-LDH. Taken together, the data presented above reveal that charge-separation and -transfer efficiency follows the same decreasing order, namely: $Ni_{76}Fe_{24}$-LDH-et-1.50 > $Ni_{76}Fe_{24}$-LDH-et-0.96 > $Ni_{76}Fe_{24}$-LDH-et-2.64 > $Ni_{76}Fe_{24}$-LDH. Intriguingly, this order is consistent with that observed for photocatalytic NO-removal efficiency, which suggests that enhanced charge separation and transfer in defective LDH is a major factor responsible for its superior photocatalytic performance. Given that $Ni_{76}Fe_{24}$-LDH-et-2.64 contains the largest number of vacancies but does not exhibit optimal charge-carrier separation and transfer, we infer that an excessive number of vacancies is detrimental [42]. Cao and coworkers also reported similar observations [43].

$OH_v$ sites have been documented to play critical roles in a variety of catalytic systems [44], with studies demonstrating that $OH_v$-exposed Lewis acidic sites strongly adsorb and activate reactants. $Fe^{3+}$ and $Ni^{2+}$, which potentially serve as reactive centers that adsorb both NO and $O_2$, are exposed in $Ni_{76}Fe_{24}$-LDH-et-*x* due to the formation of $OH_v$. To confirm this speculation, NO adsorption

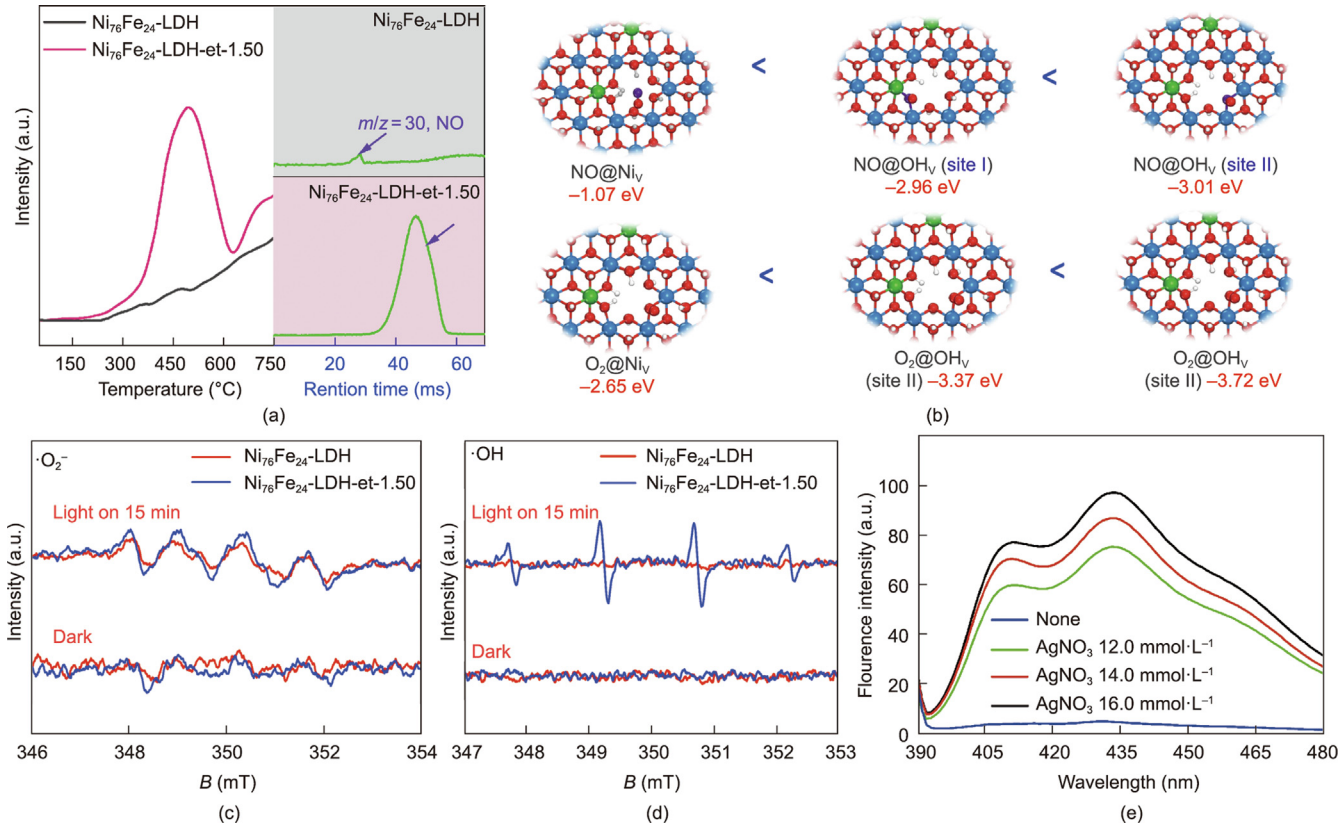


**Fig. 5.** (a) NO TPD-MS for $Ni_{76}Fe_{24}$-LDH and $Ni_{76}Fe_{24}$-LDH-et-1.50; (b) DFT calculations on the adsorption energies of NO and $O_2$ at the $Ni_v$, $OH_v$ site I and $OH_v$ site II of NiFe-LDH-et. Electron spin resonance (ESR) analyses for the ROS generated on $Ni_{76}Fe_{24}$-LDH and $Ni_{76}Fe_{24}$-LDH-et-1.50: (c) methanol dispersion for $^{\bullet}O_2^-$ and (d) aqueous dispersion for $^{\bullet}OH$; (e) $AgNO_3$ content-dependent PL spectra of the acetonitrile solution containing $Ni_{76}Fe_{24}$-LDH-et-1.50 after visible-light illumination.

on $Ni_{76}Fe_{24}$-LDH and $Ni_{76}Fe_{24}$-LDH-et-1.50 was examined by temperature programmed desorption (TPD)–mass spectrometry (TPD-Mass; AutoChem1 II 2920, Micromeritics, USA), while NO- and $O_2$-adsorption energies on defective LDH were calculated using DFT and compared. Fig. 5(a) reveals that $Ni_{76}Fe_{24}$-LDH-et-1.50 exhibits a considerably larger desorption peak in the 450–700 °C temperature range than $Ni_{76}Fe_{24}$-LDH, and MS confirmed that this peak corresponds to NO desorption, suggesting that NO is more efficiently adsorbed by defective LDH. The DFT results displayed in Fig. 5(b) reveal that the $OH_v$ site has a larger affinity for both NO and $O_2$ compared to the $Ni_v$ site. Furthermore, Furthermore, the $OH_v$ site II that exposes $Fe^{3+}$ and $Ni^{2+}$ binds more strongly with NO and $O_2$, in compared to the $OH_v$ site I that only exposes $Ni^{2+}$. It is suggested that the exposed $Fe^{3+}$ can promote the NO and $O_2$ adsorption. Similar observations were reported by Yang et al. [45].

Electron–hole pairs are formed in a photocatalyst when irradiated with light; these species can directly oxidize pollutants or trigger the formation of ROS, such as •OH or $•O_2^-$, that mineralize pollutants [46]. We first used electron spin resonance (ESR; EMX PLUS, Bruker, Germany) spectroscopy to identify the ROS formed on $Ni_{76}Fe_{24}$-LDH and $Ni_{76}Fe_{24}$-LDH-et-1.50, the results of which are shown in Fig. 5(c). Both $Ni_{76}Fe_{24}$-LDH and $Ni_{76}Fe_{24}$-LDH-et-1.05 produce $•O_2^-$ via the $e^- + O_2 \rightarrow •O_2^-$ reaction under visible light; however, the latter produces more. Fig. 5(d) shows that only $Ni_{76}Fe_{24}$-LDH-et-1.50 produces •OH in aqueous solution via the known $h^+ + H_2O \rightarrow •OH + H^+$ reaction under visible light. These EPR results show that a larger number of electron–hole pairs are generated in $Ni_{76}Fe_{24}$-LDH-et-1.50. More importantly, the holes formed in $Ni_{76}Fe_{24}$-LDH-et-1.50 are sufficiently oxidative to transform $H_2O$ into •OH. The $OH^-$ in LDH reportedly replaces $H_2O$ as the •OH precursor; consequently, LDH-based photocatalyts usually perform highly in an $H_2O$-deficint atmospheric environment. To affirm that the $OH^-$ in $Ni_{76}Fe_{24}$-LDH-et-1.50 is available for •OH production, we illuminated the photocatalyst in $H_2O$-free acetonitrile, with $AgNO_3$ and TA introduced to trap photoexcited electrons and the generated •OH (TA reacts with •OH to form TAOH), respectively. Fig. 5(e) displays $AgNO_3$-content-dependent fluorescence spectra of the solution following visible-light illumination for 0.5 h. The inclusion of $AgNO_3$ and TA led to two characteristic fluorescence peaks at 410 and 431 nm that are assigned to TAOH. Furthermore, they become more intense as more $AgNO_3$ is included. The results confirm that the $OH^-$ in $Ni_{76}Fe_{24}$-LDH-et-1.50 is available for producing •OH. This feature is significant, as it contributes to photocatalytic NO oxidation even in an $H_2O$-deficient gaseous atmosphere. Taken together, the above results demonstrate that ROS species, including $•O_2^-$ and •OH, are generated and then photocatalytically oxidize NO.

We next examined the evolution of intermediate products during the reaction over $Ni_{76}Fe_{24}$-LDH and $Ni_{76}Fe_{24}$-LDH-et-1.50 by *in-situ* DRIFTS to gain further insight into the photocatalytic NO-oxidation process on defective LDH. The spectra presented in Figs. 6(a) and (b) show that NO is more intensely adsorbed by

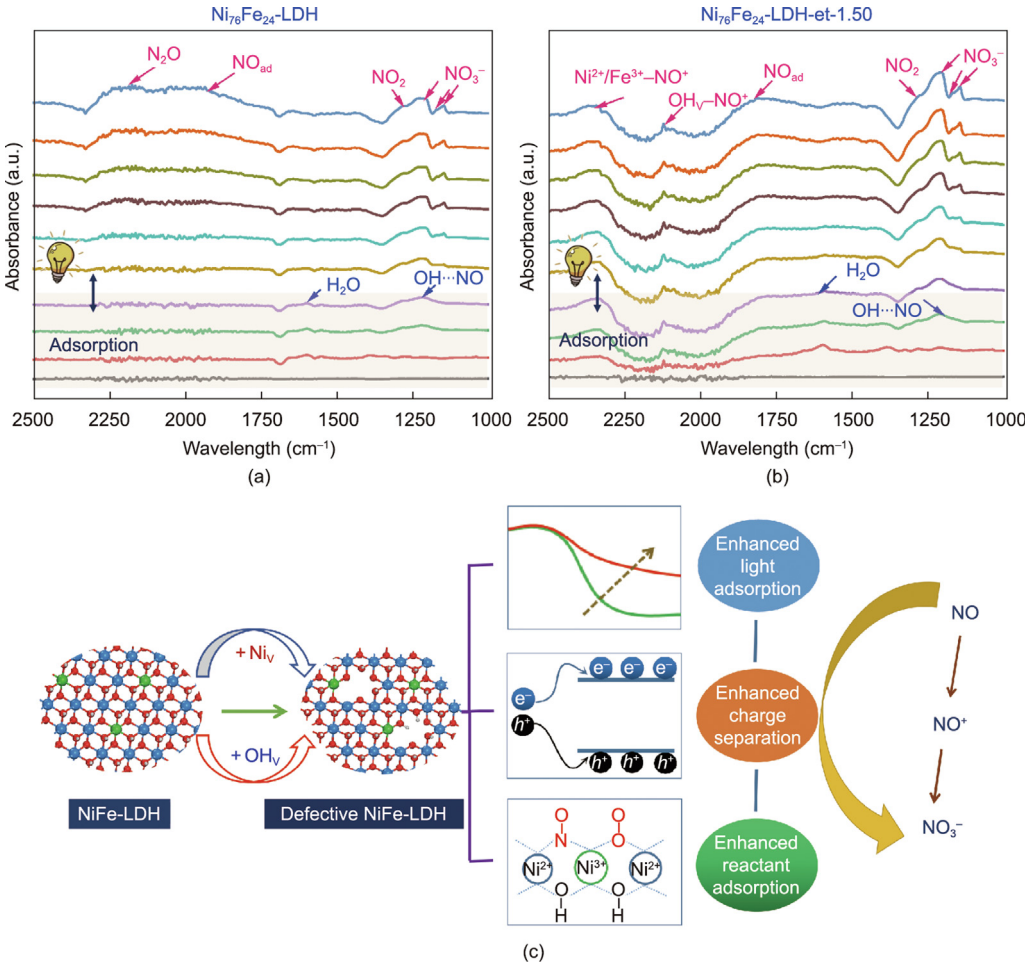


**Fig. 6.** *In-situ* DRIFTS spectra of the photocatalytic NO oxidation on (a) $Ni_{76}Fe_{24}$-LDH and (b) $Ni_{76}Fe_{24}$-LDH-et-1.50 under the dark and the simulated sunlight (the peak assignments for N-contained species were presented in Table S3 in Appendix A). (c) Schematical illustration of the roles played by the $Ni_v$ and $OH_v$ in NiFe-LDH in the photocatalytic NO oxidation.

$Ni_{76}Fe_{24}$-LDH-et than $Ni_{76}Fe_{24}$-LDH. More intriguingly, NO molecules are primarily adsorbed via hydrogen bonding to the $OH^-$ moieties on $Ni_{76}Fe_{24}$-LDH, while they are adsorbed at Lewis acidic sites (i.e., $Fe^{3+}$ and $Ni^{2+}$ at $OH_v$ sites) on $Ni_{76}Fe_{24}$-LDH-et-1.50. These results are also consistent with the TPD-MS and DFT results shown in Fig. 5. Intriguingly, the NO adsorbed at Lewis acidic sites is converted into $NO^+$, which is reportedly oxidized to $NO_3^-$ without the involvement of an $NO_2$ or $N_2O$ intermediate [34,47]. Therefore, we believe that the Lewis acidic sites contribute to alleviating $NO_2$ production on defective LDH. Figs. 6(a) and (b) also show that while both $NO_3^-$ and $NO_2$ species are resolved when illuminated by light, $NO_3^-$ increasingly accumulates with increasing reaction time. In addition, $Ni_{76}Fe_{24}$-LDH-et-1.50 exhibited a higher $NO_3^-$ yield, consistent with its higher photocatalytic activity for the oxidation of NO.

A clearer picture of the origin of the enhanced photocatalytic ability of defective NiFe-LDH toward the oxidation of NO is provided by the discussion presented above. Fig. 6(c) schematically shows that the $N_2H_4$-driven etching process triggers the formation of $Ni_v$ and $OH_v$ on the LDH; these dual vacancies promote both light adsorption and charge-carrier separation, leading to the enhanced production of ROS, including $^{\bullet}O_2^-$ and $^{\bullet}OH$. Notably, the $OH^-$ on LDH is an effective replacement for $H_2O$ during the production of $^{\bullet}OH$, which endows the LDH with steady photocatalytic performance in $H_2O$-deficient atmospheric environments. Lewis acidic sites, particularly exposed $Fe^{3+}$ at $OH_v$ sites, play important roles in the photocatalytic NO-oxidation process; they have strong affinities for NO and contribute to the accumulation of NO on the LDH. More importantly, the adsorbed NO is converted into $NO^+$ that is subsequently oxidized to $NO_3^-$ without the involvement of any $NO_2$ intermediate, thereby alleviating any risks associated with its production and emission.

## 4. Conclusions

We developed a facile $N_2H_4$-driven etching approach for preparing dual $Ni_v$- and $OH_v$-containing NiFe-LDH-et photocatalysts. In contrast to the inertness of pristine LDH, NiFe-LDH-et actively removes NO when illuminated by visible light. $Ni_{76}Fe_{24}$-LDH-et etched in 1.50 $mmol{\cdot}L^{-1}$ $N_2H_4$ solution removed 32.8% of the NO in continuously flowing air under visible light. The mechanistic study revealed that the introduction of dual vacancies improved charge separation and transfer within the LDH, leading to intensified production of ROS ($^{\bullet}O_2^-$ and $^{\bullet}OH$); they also triggered the formation of Lewis acidic sites ($Fe^{3+}$ and $Ni^{2+}$ exposed at $OH_v$) that have high NO and $O_2$ affinities. *In-situ* spectroscopic studies verified that NO is preferably adsorbed at Lewis acidic sites, particularly exposed $Fe^{3+}$. Notably, NO transforms into $NO^+$ that is directly oxidized to $NO_3^-$ without involving any of the more-toxic $NO_2$ intermediate. This study provides new perspectives for the development of efficient and durable visible-light-responsive LDH photocatalysts for the abatement of air pollution.

## Acknowledgement

The present work is financially supported by the National Natural Science Foundation of China (22176019 and 51978110), and the Science and Technology Research Program of Chongqing Municipal Education Commission (KJQN201800829, KJZD-K202000802, and KJQN201900837).

## Compliance with ethics guidelines

Xiaoyu Li, Xiaoshu Lv, Jian Pan, Peng Chen, Huihui Peng, Yan Jiang, Haifeng Gong, Guangming Jiang, and Li'an Hou declare that they have no conflict of interest or financial conflicts to disclose.

## Appendix A. Supplementary data

Supplementary data to this article can be found online at https://doi.org/10.1016/j.eng.2023.06.017.

## References

[1] Skalska K, Miller JS, Ledakowicz S. Trends in $NO_x$ abatement: a review. Sci Total Environ 2010;408(19):3976–89.
[2] Li N, Wang C, Zhang K, Lv H, Yuan M, Bahnemann DW. Progress and prospects of photocatalytic conversion of low-concentration NO. Chin J Catal 2022;43(9):2363–87.
[3] Cui W, Li J, Dong F. Optimizing the gas-solid photocatalytic reactions for air purification. ACS ES&T Eng 2022;2(6):1103–15.
[4] Zhao K, Sun X, Wang C, Song X, Wang F, Li K, et al. Supported catalysts for simultaneous removal of $SO_2$, $NO_x$, and $Hg^0$ from industrial exhaust gases: a review. Chin Chem Lett 2021;32(10):2963–74.
[5] Zheng Y, Chen Y, Gao B, Lin B, Wang X. Phosphorene-based heterostructured photocatalysts. Engineering 2021;7(7):991–1001.
[6] Chen WQ, Li LY, Li L, Qiu WH, Tang L, Xu L, et al. MoS2/ZIF-8 hybrid materials for environmental catalysis: solar-driven antibiotic-degradation engineering. Engineering 2019;5(4):755–67.
[7] Buzzetti L, Crisenza GEM, Melchiorre P. Mechanistic studies in photocatalysis. Angew Chem Int Ed 2019;58(12):3730–47.
[8] Zhu H, Yuan X, Yao Q, Xie J. Shining photocatalysis by gold-based nanomaterials. Nano Energy 2021;88:106306.
[9] Wu C, Xing Z, Yang S, Li Z, Zhou W. Nanoreactors for photocatalysis. Coord Chem Rev 2023;477:214939.
[10] Yang W, Ren Q, Zhong F, Wang Y, Wang J, Chen R, et al. Promotion mechanism of -OH group intercalation for $NO_x$ purification on BiOI photocatalyst. Nanoscale 2021;13(48):20601–8.
[11] Yan Q, Hou X, Liu G, Li Y, Zhu T, Xin Y, et al. Recent advances in layered double hydroxides (LDHs) derived catalysts for selective catalytic reduction of NOx with NH3. J Hazard Mater 2020;400:123260.
[12] Jerome MP, Alahmad FA, Salem MT, Tahir M. Layered double hydroxide (LDH) nanomaterials with engineering aspects for photocatalytic CO2 conversion to energy efficient fuels: fundamentals, recent advances, and challenges. J Environ Chem Eng 2022;10(5):108151.
[13] Zhang S, Zhao Y, Shi R, Zhou C, Waterhouse GIN, Wu LZ, et al. Efficient photocatalytic nitrogen fixation over Cuδ+-modified defective ZnAl-layered double hydroxide nanosheets. Adv Energ Mater 2020;10(8):1901973.
[14] Lv X, Zhang J, Dong X, Pan J, Zhang W, Wang W, et al. Layered double hydroxide nanosheets as efficient photocatalysts for NO removal: band structure engineering and surface hydroxyl ions activation. Appl Catal B 2020;277:119200.
[15] Zou J, Wang Z, Guo W, Guo B, Yu Y, Wu L. Photocatalytic selective oxidation of benzyl alcohol over ZnTi-LDH: the effect of surface OH groups. Appl Catal B 2020;260:118185.
[16] Dong XA, Cui Z, Sun Y, Dong F. Humidity-independent photocatalytic toluene mineralization benefits from the utilization of edge hydroxyls in layered double hydroxides (LDHs): a combined operando and theoretical investigation. ACS Catal 2021;11(13):8132–9.
[17] Zhang X, Zhao Y, Zhao Y, Shi R, Waterhouse GIN, Zhang T. A simple synthetic strategy toward defect-rich porous monolayer NiFe-layered double hydroxide nanosheets for efficient electrocatalytic water oxidation. Adv Energy Mater 2019;9(24):1900881.
[18] Miao W, Wang Y, Liu Y, Qin H, Chu C, Mao S. Persulfate-induced three coordinate nitrogen (N3C) vacancies in defective carbon nitride for enhanced photocatalytic H2O2 evolution. Engineering 2023;25(6):214–21.
[19] Wu Q, Jia Y, Liu Q, Mao X, Guo Q, Yan Y, et al. Ultra-dense carbon defects as highly active sites for oxygen reduction catalysis. Chem 2022;8(10):2715–33.
[20] Liu G, Tang Z, Gu X, Li N, Lv H, Huang Y, et al. Boosting photocatalytic nitrogen reduction to ammonia by dual defective -C N and K-doping sites on graphitic carbon nitride nanorod arrays. Appl Catal B 2022;317:121752.
[21] He Y, Lei Q, Li C, Han Y, Shi Z, Feng S. Defect engineering of photocatalysts for solar-driven conversion of $CO_2$ into valuable fuels. Mater Today 2021;50:358–84.
[22] Li X, Li H, Huang Y, Cao J, Huang T, Li R, et al. Exploring the photocatalytic conversion mechanism of gaseous formaldehyde degradation on $TiO_{2-x}$-$O_V$ surface. J Hazard Mater 2022;424:127217.
[23] Yuan R, Wang M, Liao L, Hu W, Liu Z, Liu Z, et al. 100% $N_2O$ inhibition in photocatalytic $NO_x$ reduction by carbon particles over $Bi_2WO_6/TiO_2$ Z-scheme heterojunctions. Chem Eng J 2023;453:139892.
[24] Wang H, Li K, Li J, Sun Y, Dong F. Photochemical transformation pathways of nitrates from photocatalytic $NO_x$ oxidation: implications for controlling secondary pollutants. Environ Sci Technol Lett 2021;8(10):873–7.
[25] Wang H, Sun Y, Dong F. Insight into the overlooked photochemical decomposition of atmospheric surface nitrates triggered by visible light. Angew Chem Int Ed 2022;61(43):e202209201.
[26] Liu L, Ouyang P, Li Y, Duan Y, Dong F, Lv K. Insight into the mechanism of deep NO photooxidation by bismuth tantalate with oxygen vacancies. J Hazard Mater 2022;439:129637.

[27] Yu Y, Dong X, Chen P, Geng Q, Wang H, Li J, et al. Synergistic effect of Cu single atoms and Au–Cu alloy nanoparticles on $TiO_2$ for efficient $CO_2$ photoreduction. ACS Nano 2021;15(9):14453–64.
[28] Wang Q, Chen L, Guan S, Zhang X, Wang B, Cao X, et al. Ultrathin and vacancy-rich CoAl-layered double hydroxide/graphite oxide catalysts: promotional effect of cobalt vacancies and oxygen vacancies in alcohol oxidation. ACS Catal 2018;8(4):3104–15.
[29] Bai L, Lee S, Hu X. Spectroscopic and electrokinetic evidence for a bifunctional mechanism of the oxygen evolution reaction. Angew Chem Int Ed 2021;60 (6):3095–103.
[30] Louie MW, Bell AT. An investigation of thin-film Ni-Fe oxide catalysts for the electrochemical evolution of oxygen. J Am Chem Soc 2013;135 (33):12329–37.
[31] Bantignies JL, Deabate S, Righi A, Rols S, Hermet P, Sauvajol JL, et al. New insight into the vibrational behavior of nickel hydroxide and oxyhydroxide using inelastic neutron scattering, far/mid-infrared and raman spectroscopies. J Phys Chem C 2008;112(6):2193–201.
[32] Bernard MC, Cortes R, Keddam M, Takenouti H, Bernard P, Senyarich S. Structural defects and electrochemical reactivity of β-Ni(OH)2. J Power Sources 1996;63(2):247–54.
[33] Peng L, Yang N, Yang Y, Wang Q, Xie X, Sun-Waterhouse D, et al. Atomic cation-vacancy engineering of NiFe-layered double hydroxides for improved activity and stability towards the oxygen evolution reaction. Angew Chem Int Ed 2021;60(46):24612–9.
[34] Song X, Jiang W, Cai Z, Yue X, Chen X, Dai W, et al. Visible light-driven deep oxidation of NO and its durability over Fe doped BaSnO3: the NO+ intermediates mechanism and the storage capacity of Ba ions. Chem Eng J 2022;444:136709.
[35] Zhao K, Qi J, Yin H, Wang Z, Zhao S, Ma X, et al. Efficient water oxidation under visible light by tuning surface defects on ceria nanorods. J Mater Chem A Mater Energy Sustain 2015;3(41):20465–70.
[36] Hu Z, Li X, Zhang S, Li Q, Fan J, Qu X, et al. $Fe_1/TiO_2$ Hollow microspheres: Fe and Ti dual active sites boosting the photocatalytic oxidation of NO. Small 2020;16(47):2004583.
[37] Ruggieri M, Plaia A. An aggregate AQI: comparing different standardizations and introducing a variability index. Sci Total Environ 2012;420:263–72.
[38] Xiao M, Wang S, Thaweesak S, Luo B, Wang L. Tantalum (oxy)nitride: narrow bandgap photocatalysts for solar hydrogen generation. Engineering 2017;3 (3):365–78.
[39] Jiang L, Yang J, Yuan X, Guo J, Liang J, Tang W, et al. Defect engineering in polymeric carbon nitride photocatalyst: synthesis, properties and characterizations. Adv Colloid Interface Sci 2021;296:102523.
[40] Ahsan MA, Puente Santiago AR, Hong Y, Zhang N, Cano M, Rodriguez-Castellon E, et al. Tuning of trifunctional NiCu bimetallic nanoparticles confined in a porous carbon network with surface composition and local structural distortions for the electrocatalytic oxygen reduction, oxygen and hydrogen evolution reactions. J Am Chem Soc 2020;142(34):14688–701.
[41] Cheng G, Tan X, Song X, Chen X, Dai W, Yuan R, et al. Visible light assisted thermocatalytic reaction of CO + NO over Pd/LaFeO3. Appl Catal B 2019;251:130–42.
[42] Zhao Y, Zheng L, Shi R, Zhang S, Bian X, Wu F, et al. Alkali etching of layered double hydroxide nanosheets for enhanced photocatalytic $N_2$ reduction to $NH_3$. Adv Energy Mater 2020;10(34):2002199.
[43] Cao J, Zhang J, Dong XA, Fu H, Zhang X, Lv X, et al. Defective borate-decorated polymer carbon nitride: enhanced photocatalytic NO removal, synergy effect and reaction pathway. Appl Catal B 2019;249:266–74.
[44] Lv X, Jiang K, Wu H, Ao L, Hu L, Li X, et al. Defective layered double hydroxide nanosheet boosts electrocatalytic hydrodechlorination reaction on supported palladium nanoparticle. ACS ES&T Water 2022;2(8):1451–60.
[45] Yang W, Feng X, Chen X, Wu C, Wang F, Gao Z, et al. Understanding trends in the NO oxidation activity of single-atom catalysts. J Environ Chem Eng 2022;10(6):108744.
[46] Wu L, An S, Song YF. Heteropolyacids-immobilized graphitic carbon nitride: highly efficient photo-oxidation of benzyl alcohol in the aqueous phase. Engineering 2021;7(1):94–102.
[47] Liao J, Cui W, Li J, Sheng J, Wang H, Dong XA, et al. Nitrogen defect structure and NO+ intermediate promoted photocatalytic NO removal on H2 treated g-C3N4. Chem Eng J 2020;379:122282.